Journal of
Applied Remote Sensing

Point response function of the Clouds and Earth Radiant Energy System scanning radiometer

G. Louis Smith
Janet L. Daniels
Kory J. Priestley
Susan Thomas

SPIE

Point response function of the Clouds and Earth Radiant Energy System scanning radiometer

G. Louis Smith,[a,*] Janet L. Daniels,[a] Kory J. Priestley,[b] and Susan Thomas[a]
[a]Science Systems Applications Inc., 1 Executive Drive, Hampton, Virginia 23666
[b]Science Directorate, Langley Research Center, NASA, Hampton, Virginia 23681

Abstract. An overview of work related to the point response function (PRF) of the Clouds and Earth Radiant Energy System (CERES) scanning radiometer is presented. The aspects of the CERES design that affect the PRF are described, and then the design of the PRF is explained. The PRF was designed by shaping the field of view so as to minimize the blur plus alias errors of the radiance field reconstructed from the CERES measurements. The design is conducted in the Fourier domain. The PRF can then be computed by transforming the resulting transfer function to the physical domain. Alternatively, the PRF can be computed in the physical plane. The PRF of each model of the CERES instrument has been tested in the Radiation Calibration Facility by use of a PRF source and compared well with prediction. CERES instruments are aboard the Terra, Aqua, and Suomi-NPP spacecraft. In orbit, lunar observations are used to validate the PRF. These results showed nominal performance except for the longwave window channel of flight model 2, for which a region of anomalously high sensitivity was found. [DOI: 10.1117/1.JRS.8.084991]

Keywords: point response function; Clouds And Earth Radiant Energy System; Terra; Aqua; Suomi-NPP; image processing.

Paper 13428SS received Nov. 1, 2013; revised manuscript received Feb. 27, 2014; accepted for publication Mar. 3, 2014; published online Apr. 1, 2014.

1 Introduction

The Clouds And Earth Radiant Energy System (CERES) project has two major objectives: to measure radiances so that the radiation fluxes at the top of the atmosphere (TOA) can be retrieved and to compute the radiation fluxes at the surface of the Earth and through the atmosphere.[1] The CERES instrument is a scanning radiometer, which scans from one limb of the Earth to the other. There are three channels: a total channel for measuring all radiation leaving Earth from 0.2 to 50μ, a shortwave channel for measuring solar radiation between 0.2 and 5.0μ reflected by the Earth, and a longwave window channel for measuring radiation in the 8- to 12-μ window. The effect of radiation from a given point at TOA on the measurement of a channel is defined as its point response function (PRF). The PRF determines the fidelity with which the geographic distribution of the radiation field, or image, is determined by the measurements. The objective of the PRF design is to optimize the fidelity of this image with the observed field. The PRF is determined by the construction of the telescope and electronics of the channel.

CERES flight models (FM) 1 and 2 are aboard the Terra spacecraft and have operated since February 2000. FM-3 and FM-4 are on the Aqua spacecraft and have operated since June 2002. FM-5 is aboard the Suomi-NPP spacecraft, which was placed in orbit in October 2011.

To compute the radiation fluxes at the surface and through the atmosphere, data from MODIS are used with data from CERES aboard Terra and Aqua and data from VIIRS are used with CERES data from Suomi-NPP.[2–4] These imagers provide information about cloud fraction and height or, if clear, the surface temperature. The MODIS and VIIRS imager data are of much higher resolution than CERES, as sketched in Fig. 1. It is necessary to weight the surface

*Address all correspondence to: G. Louis Smith, George.l.smith@nasa.gov

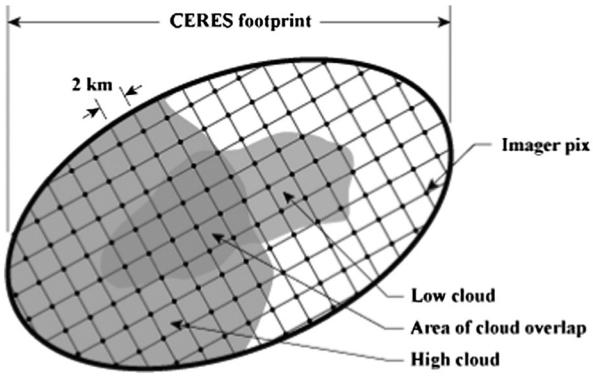

Fig. 1 Schematic of CERES footprint with imager pixels.

and atmosphere results from the imager at points within the CERES field of view (FOV) the same as does the CERES. Thus, one must know the CERES PRF. The PRF is also needed so that the centroid position can be determined, from which the pixels' locations can be computed.

The construction of the sensors is first described. The rationale and analysis for the design of the CERES PRF is then explained. Testing of the PRF in the Radiation Calibration Facility (RCF),[5] which was done for each flight model, is discussed. Finally, validation of the PRF in orbit by use of lunar observations is described.

2 Description of Sensors

Each of the three channels of the CERES instrument[6] has a sensor mounted on a scan beam, which rotates in elevation angle from limb to limb. Each sensor has a Cassegrain telescope, which gathers radiance onto the detector, as shown in Fig. 2. At the focal plane of the telescope, a field stop is located, which determines the FOV.[7] The detector integrates the radiance over the area of the scene within the instantaneous FOV. Figure 3 shows the final FOV design; the shape and size are determined by the following analysis. Spherical mirrors are used and spot diagrams show the effects of spherical aberrations. For the telescope to get sufficient irradiance onto the detector to create a measurement with the required signal-to-noise ratio, the area of the aperture of the field stop must be at least 2.5 square degrees, which corresponds to a 1.58-deg square.

The detector is connected through a bridge circuit to a passive detector, which is on a heat sink behind the active detector in a thermally controlled environment. The detectors have a first-order time response with a response time of 10 ms. The signal is smoothed by a four-pole Bessel

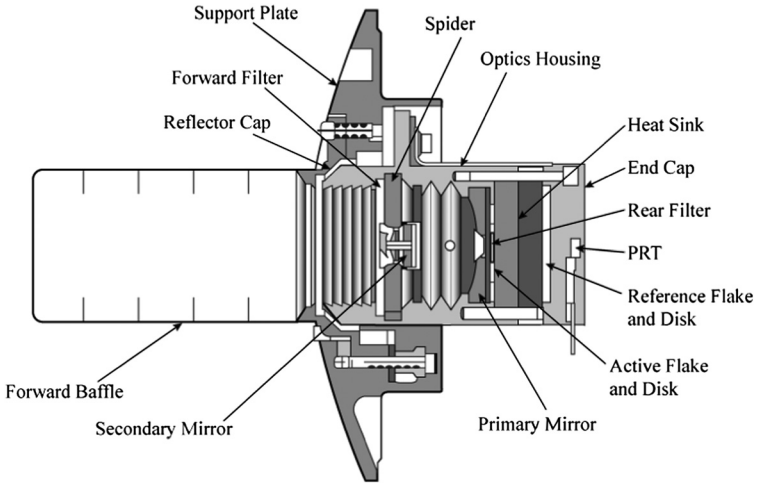

Fig. 2 Cross section of CERES sensor.

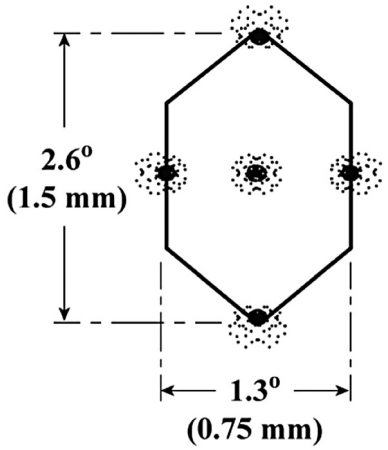

Fig. 3 Field of view of CERES instrument with spot diagrams on field stop.

filter to attenuate noise and is then sampled every 10 ms. Figure 4 is a block diagram of the system. The instrument scan rate is nominally 63.5 deg/s.

3 Design of Point Response Function

The following parameters affect the PRF: FOV size and shape, time response of the detectors, signal conditioning circuit (Bessel filter) by-pass frequency, and sampling rate. The Bessel filter parameters were selected by electronics considerations.

The shape of the CERES FOV was designed following the method of Huck et al.[8–10] for the FOV of the Earth radiation budget scanning radiometer. The configuration and dimensions of this aperture were selected to optimize the fidelity of the image, which can be reconstructed from the measurements. This optimization is performed in the Fourier domain, in which the PRF becomes the system transfer function and will be discussed later in this paper.

3.1 *Optimization Criteria*

As the instrument scans across the Earth from limb to limb, the FOV at the TOA grows, so that the fidelity of the reconstructed image with the observed field varies. The data near nadir are the best for science application because as the instrument scans from nadir toward the limb, three-dimensional aspects of clouds cause the apparent cloudiness to increase, with increasing difficulty to compute cloud features properly. Consequently, the parameters were selected to optimize the image fidelity near nadir.

To optimize the PRF, it is assumed that the measurements will be used to reproduce the original field. Although this is not the primary use of the data, it is assumed that if the design satisfies this criterion, the data will provide coverage of the region so as to compute a near-optimal value for the mean flux over the region. The design criterion is that the square of the difference between the reconstructed image and the observed field be minimal. For this purpose, it is assumed that the image of the measured radiance field is created in the Fourier domain.

The detail in the reproduced flux field is limited in the scan direction by the sampling rate and in the orbit track direction by distance between scan lines, as stated by Shannon's sampling theorem. The distance between scan lines was determined by the scan rate, which was set by mechanical considerations including lifetime, and the spacecraft speed and altitude. Any

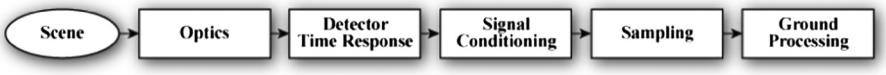

Fig. 4 Block diagram of scanning radiometer system.

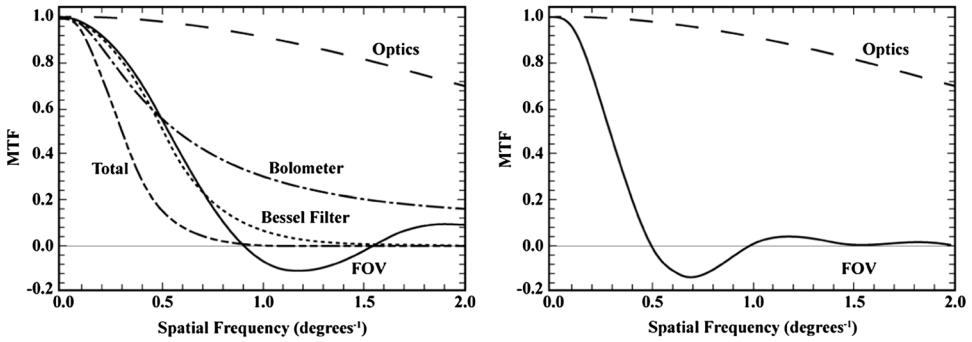

Fig. 5 Component transfer functions and system (total) transfer functions for scan direction (a) and direction normal to scan (b).

spatial frequencies shorter than the distance between samples or scan lines will alias into spurious features in the reproduced field, so the sensor should have low response to these frequencies. However, as the sensor response decreases before the sampling rate limit, the spatial frequencies slower than the sampling rate will be diminished by the sensor, resulting in blurring. A scanning radiometer will blur features with size on the order of the field of view and also due to time responses of the sensor system. The total variance of error σ_t^2 between the image, which can be reproduced from the data and the original scene, is

$$\sigma_t^2 = \sigma_b^2 + \sigma_a^2 + \sigma_h^2 + \sigma_n^2, \tag{1}$$

where the terms on the right hand side are variances of errors due to blur, aliasing of high frequencies into low frequencies, high frequencies that are not reproduced, and noise.[10] The sampling rate in the scan direction and the distance between scans are fixed by other design considerations. The condition to provide the best reproduction of the field is to minimize the sum of the blur and alias errors. The error due to high spatial frequency components σ_h^2 is determined by the sampling frequency and the distance between scan lines, is not affected by the other design parameters, and is disregarded. The noise term is minimized by the electronic filter and is disregarded.

The analysis is carried out in the Fourier domain. The measurements are sampled and digitized; thus features smaller than the distance between samples cannot be recovered from the data, as stated by Shannon's theorem.

Katzberg et al.[10] and Huck et al.[9] showed that a hexagonal FOV is very well suited to sample a two-dimensional image. The beauty of the hexagon appears in the Fourier domain. The points of the hexagon cause the transfer function (TF) to decrease rapidly with increasing frequency in the cross-scan direction. High-frequency waves in the scan direction are quickly diminished by the time response of the detector and by the four-pole Bessel filter.

3.2 *Analysis*

A Fourier wave is expressed in the sensor coordinate system with spatial frequencies of ω_x in the scan direction and ω_y in the normal direction, and its amplitude is denoted as $A(\omega_x, \omega_y)$. The radiance at a point x, y is $A(\omega_x, \omega_y)e^{i(\omega_x x + \omega_y y)}$. The response of the sensor is written as $A(\omega_x, \omega_y)T_s(\omega_x, \omega_y)$, where $T_s(\omega_x, \omega_y)$ is the transfer function (TF) of the sensor. The system TF is the product of the TFs of the individual blocks of Fig. 4. The blur error of this wave is $A(\omega_x, \omega_y)[1 - T_s(\omega_x, \omega_y)]$. For a two-dimensional field, the variance of blur error is the expected contributions of all frequencies within the domain, which is sampled.

$$\sigma_b^2 = \int_{-\frac{1}{2Y}}^{\frac{1}{2Y}} \int_{-\frac{1}{2X}}^{\frac{1}{2X}} \mathrm{d}\omega_x \mathrm{d}\omega_y S(\omega_x, \omega_y)|1 - T_s(\omega_x, \omega_y)|^2, \tag{2}$$

and the spectrum

$$S(\omega_x, \omega_y) = E\{A(\omega_x, \omega_y)A^*(\omega_x, \omega_y)\} \tag{3}$$

is the expected value of the squared amplitude of all waves. The rectangular region in the Fourier domain over which this integration is performed is denoted R and the remainder of the plane is denoted as R'. The variance of aliasing error is the power of the measurement beyond R.

$$\sigma_a^2 = \iint_{R'} \mathrm{d}\omega_x \mathrm{d}\omega_y S(\omega_x, \omega_y)|T_s(\omega_x, \omega_y)|^2. \tag{4}$$

For the blur and alias computations, the spectrum of the field is needed. For the design, a two-dimensional Wiener spectrum, which had been found to agree with data, was suggested by Huck et al.[8]

$$S(\Omega_x, \Omega_y) = (2\pi)^{-1}\lambda^2\sigma_M^2[1 + \lambda^2(\Omega_x^2 + \Omega_y^2)]^{-3/2}, \tag{5}$$

where λ is a characteristic distance and σ_M is the standard deviation of the field. The values $\lambda = 100$ km and $\sigma_M = 240\ W\,\mathrm{m}^{-2}$ are used. This form has been found to agree well with earth radiation budget experiment and AVHRR data over the wavelength range of 200 to 2 km, which is the range of interest. The spatial frequencies Ω_x, Ω_y are at TOA and must be transformed to the instrument coordinates ω_x, ω_y by geometric scaling.

3.3 *Analysis Results*

Manalo and Smith[11,12] performed parametric studies in which the shape of the hexagon was varied. With the shape of the field stop aperture and the time constants of the detector and electronic filter, the component or modular TFs can be computed. Figure 5 shows the results for the scan direction and for the direction normal to that. The abscissas are the spatial frequency in inverse degrees at the instrument. The scan rate is 63.5 deg /s, so there is a sample every 0.635 inverse degrees and the Nyquist limit is 0.32 inverse degrees. The blur circle TF decreases very slowly with increasing frequency and is rotationally symmetric. The detector and electronic filter time responses do not affect spatial frequencies in the directions normal to scan. The FOV shape neutralizes frequency of 0.5 inverse degrees and has a very small overshoot normal to the scan beyond 1.3 inverse degrees. In the scan direction, the FOV TF has a zero at 0.9 inverse degrees and overshoots. However, the detector and filter time responses decrease the TF in the scan direction so that the system TF is ~0 at 0.64 inverse degrees.

Figure 6 shows that the optimum is given by 2.6 deg across the points in the cross-scan direction. To have a field of view of 2.5 square degrees as required to get the signal-to-noise needed, the distance between the sides in the scan direction must be 1.3 deg, giving the FOV shown in Fig. 3. This result was duplicated independently by Gary Peterson of the TRW team. Because of the −3 power of the spatial spectrum, the spectral power near the Nyquist limit is small for this case and deviations from the optimum cause only small increases in the blur plus alias error.

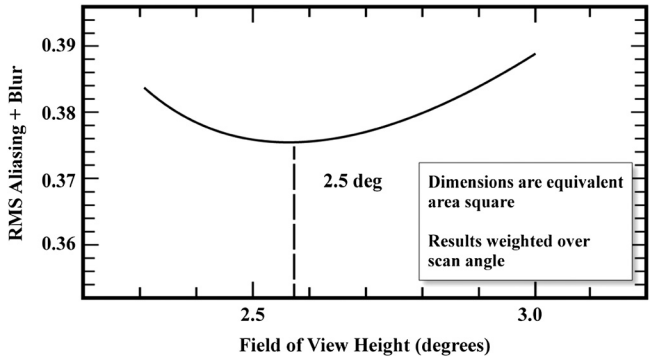

Fig. 6 Root-mean-square alias plus blur errors as function of field-of-view height (degrees) for total area of field of view of 2.5 square degrees.

3.4 *Selected Point Response Function*

With the shape of the field stop aperture and the time constants of the detector and electronic filter, the system TF is known and the PRF can be computed as the transform of the TF to the physical domain. Alternatively, the PRF can be computed in the physical domain algebraically.[13] Figure 7 shows the PRF for CERES. As the radiometer scans over a radiating point, when the point comes within the FOV, the detector time response causes the measurement to increase slowly. When the radiometer scans past the point, the measurement decreases slowly. The result is that the centroid of the measurement is behind the center of the FOV. The effect of the electronic filter is to decrease the curvature of the measurement in the scan direction and to further delay the response. This displacement of the centroid of the PRF is taken into account when geolocating the measurement. The effect of the spherical aberrations can be included by convolving the blur circle with the PRF as computed above. The result will slightly decrease the curvature of the shape, but does not affect the centroid or geolocation of the pixel.

A computer model of the CERES sensor was also developed by Haeffelin et al.[14] This model included ray tracing for the incoming radiance through the optics and numerical solution of the partial differential equations for the electric field and temperature distribution. This computer model has the advantage that deviations from the design can be easily accommodated.

4 Testing PRF in Calibration Facility

To verify that the PRF of each channel of each flight model of CERES behaves as expected, a PRF source was built and added to the RCF[5,15] so that PRF testing could be done in vacuum. A schematic of the PRF source is shown in Fig. 8. A Nerst glower provides sufficient radiance to give a good dynamic range for each of the three CERES channels. The glower is outside the vacuum chamber and a focusing mirror sends radiation from the source through a window into the vacuum. A pinhole at the focal point of the mirror eliminates any radiation not from the glower. An off-axis parabolic mirror reflects the radiation as a nearly collimated beam. Another mirror TF3 reflects the beam to the CERES instrument. The radiances in the final beam are within a cone of 0.16 deg, which is the size of the blur circle due to spherical aberrations.

The CERES scans in elevation angle to collect data in the scan direction. Figure 9 is a sample of data. The spacing of data in the scan direction is reduced by tilting TF3 in the horizontal direction (i.e., about its vertical axis), as denoted by different symbols. The cross-scan position is varied by tilting the TF3 mirror in the vertical direction (i.e., about its horizontal axis), and scans are made for several cross-scan positions to define the PRF experimentally. This has been done for each of the CERES instruments.[16–19] Figure 10 shows the predicted PRF in the left panel and the PRF for the total channel of FM-1 as measured in the Radiometric Calibration Facility in the right panel. The effect of the beam size is taken into account in the predicted PRF by convolving the beam with the analytic model with the blur circle included.

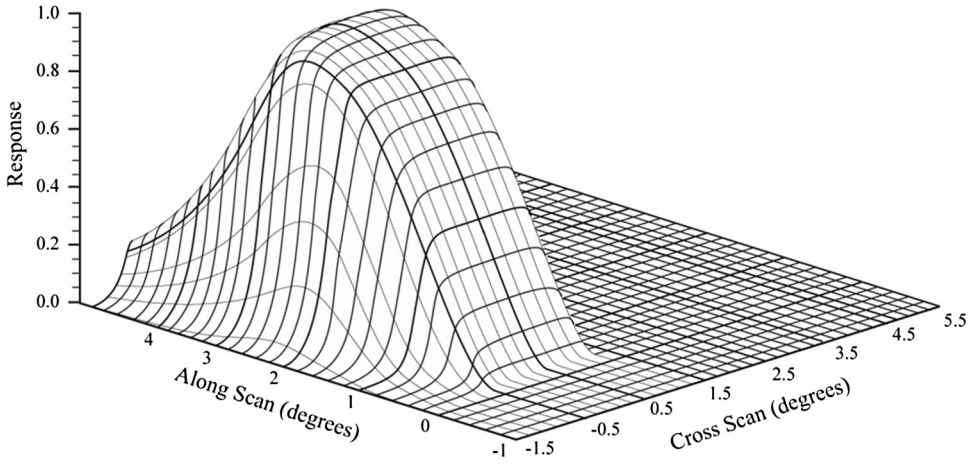

Fig. 7 CERES point response function.

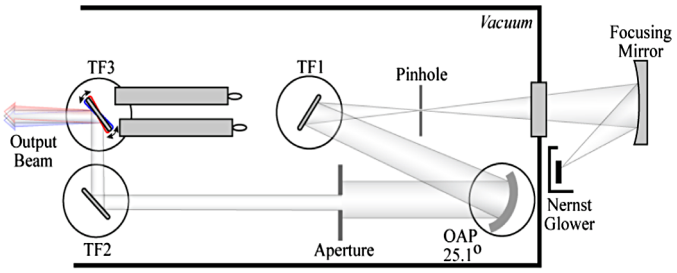

Fig. 8 Schematic of point response function source used in Radiation Calibration Facility for CERES instruments.

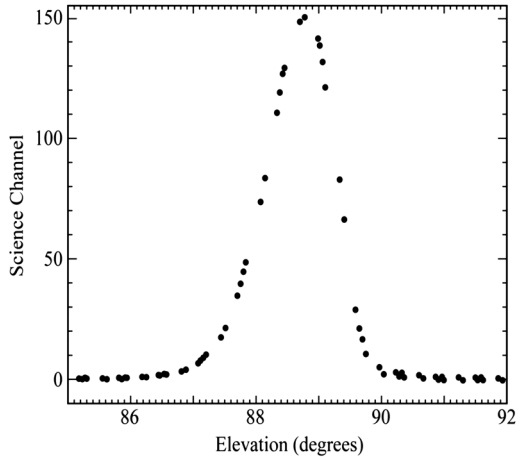

Fig. 9 Sample of data from point response function testing in Radiation Calibration Facility as CERES scans past source.

During testing of the CERES instrument in the RCF, a slow mode was found, which is on the order of a percent in magnitude and has a response time of ~300 ms.[20] This mode was found to be due to heating of the heat sink on which the detector is mounted. A numerical filter was implemented, which attenuates the effects of this mode to insignificance.[21]

5 Validating PRF in Orbit

The moon is a radiation source that can be used for validating the PRF of CERES. Figure 11 shows the image of the moon relative to the FOV of CERES. As the Terra spacecraft passes over

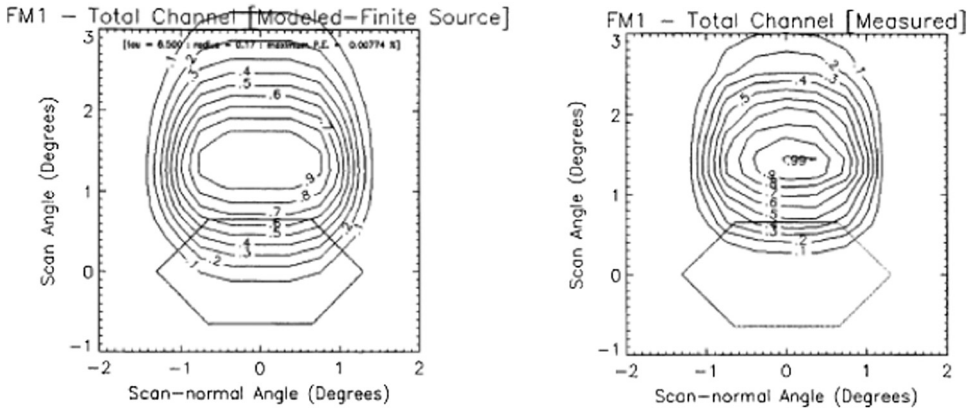

Fig. 10 (a) Computed total channel PRF, including finite size of PRF source. (b) Measured total channel for FM-1.

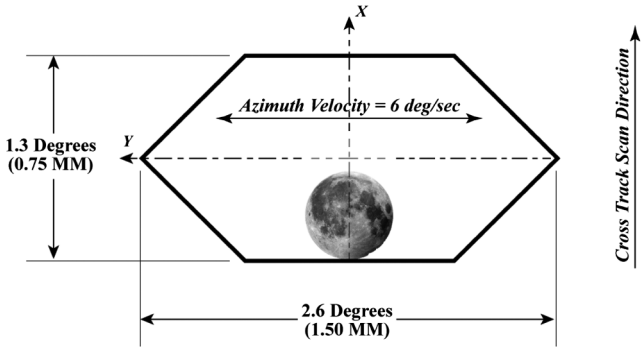

Fig. 11 Size of image of the moon in the CERES field of view.

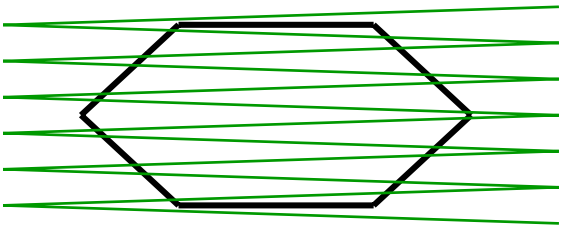

Fig. 12 Location of center of moon as CERES scans in azimuth (left and right) and the Terra Motion produces elevation change (vertical).

Antarctica when the moon is within 10 deg of being full, a rotation of CERES in azimuth will bring the moon into view of the instrument between the limb of the Earth and the instrument itself. During these opportunities, the elevation of CERES is fixed. As Terra moves along its orbit, it rotates to maintain its alignment with nadir, which causes the elevation of the moon relative to the spacecraft to slowly change. During this time, CERES rotates back and forth in azimuth to scan across the moon as the moon, as indicated in Fig. 12. The scan rate is sufficiently slow that the time response of the sensor is negligible and the static PRF is measured, i.e., the sensitivity of the sensor without effects of significant time responses of the detector and electronic filter.

Lunar observations have been made with FM-1 through FM-4 for a decade and observations have been started with FM-5, aboard Suomi-NPP. The results of these data for validating the CERES PRFs have been reported.[22,23] With the exception of one channel, these measurements showed that the static PRFs were unchanged since ground testing. Figure 13 shows the static PRFs of the three channels of FM-2. The decrease of PRF at the edges is due to the moon not being completely within the FOV. The total and shortwave channels have uniform responses within the part of the FOV within which the moon is fully inside the FOV. The longwave window channel of FM-2 has a region of anomalous high sensitivity. This effect is attributed to delamination of the detector flake from the heat sink as shown in Fig. 14. Separation of the thermistor

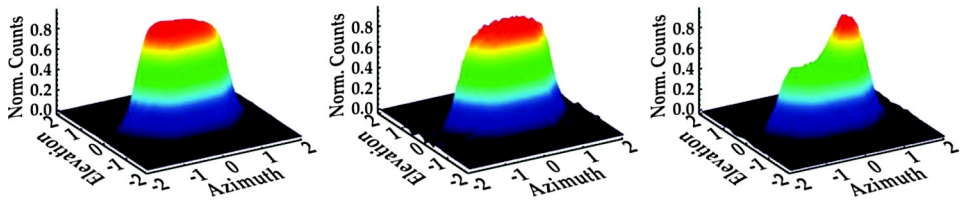

(a) total channel (b) shortwave channel (c) longwave window channel

Fig. 13 Static point response functions for FM-2 channels: (a) Total channel. (b) Shortwave channel. (c) Longwave window channel.

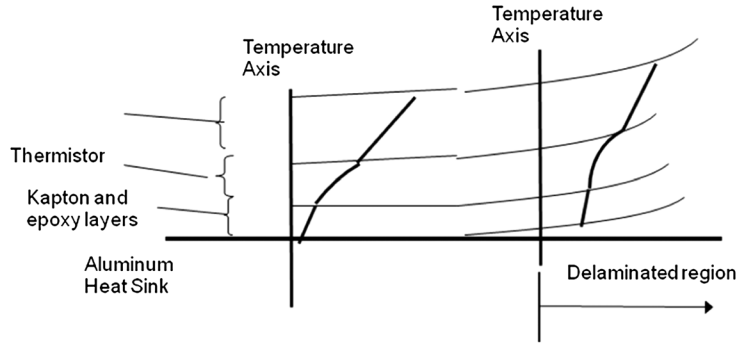

Fig. 14 Sketch showing temperature increase in thermistor flake due to delamination from heat sink.

flake from the heat sink results in loss of conduction of heat from the flake and an increased temperature, producing a higher measurement in that region than the rest of the flake. To find such problems with lunar observations was unexpected.

6 Concluding Remarks

This paper presents an overview of the CERES PRF from design to in-orbit validation. The rationale for the design must come from scientific objectives and is explained. The design concept was the same as was used for the Earth Radiation Budget Experiment scanning radiometer. The CERES PRF is optimized for the Terra and Aqua orbits.

The use of CERES measurements with data from higher-resolution instruments in the data analysis made it necessary to characterize the PRF well. A model in the physical domain was developed to complement the Fourier domain model. To verify the analytic models of the PRF, a PRF source was designed for use in the RCF to test the PRFs of CERES instruments. Data from these tests verified the computed PRF in all cases. The measurements are seen to agree well with the computed PRF.

A technique was developed to validate the PRF in orbit by use of lunar observations. This method demonstrated that the PRF has been stable over the life of the missions for FM-1 through FM-4 except for the longwave window channel of FM-2. The FM-2 longwave window detector was found to have a site for which the sensitivity is greater than the rest of the detector, which is attributed to delamination of the detector. Thus, the PRF validation also provided a check of the detector well-being.

Acknowledgments

The authors are grateful to the Science Directorate of Langley Research Centre and to the Science Mission Directorate of the Earth Science Division of NASA for the support of the CERES Project. We also thank the engineers and technicians at the Space Division of TRW (presently Northrop-Grumann) for their round-the-clock session with the RCF, the CERES Flight Operations Team at LaRC for collecting the data, and the CERES Instrument Working Group for analyzing all of the measurements.

References

1. B. R. Barkstrom, "Earth radiation budget measurements, Pre-ERBE, ERBE, and CERES," *Proc. SPIE* **1299**, 52–60 (1990), http://dx.doi.org/10.1117/12.21364.
2. B. A. Wielicki et al., "Clouds and the Earth's radiant energy system (CERES): algorithm overview," *IEEE Trans. Geosci. Remote Sens.* **36**(4), 1127–1141 (1998), http://dx.doi.org/10.1109/36.701020.
3. R. N. Green and B. A. Wielicki, "Convolution of imager cloud properties with CERES footprint point spread function (Subsystem 4.4)," http://eospso.nasa.gov/sites/default/files/atbd/atbd-cer-09.pdf (1997).

4. F. G. Rose et al., "An algorithm for the constraining of radiative transfer calculations to CERES observed broadband top of atmosphere irradiance," *J. Atmos. Oceanic Technol.* **30**(6), 1091–1106 (2013), http://dx.doi.org/10.1175/JTECH-D-12-00058.1.
5. R. B. Lee, III et al., "The clouds and the Earth's radiant energy system (CERES) sensors and preflight calibration plans," *J. Atmos. Oceanic Technol.* **13**(2), 300–313 (1996), http://dx.doi.org/10.1175/1520-0426(1996)013<0300:TCATER>2.0.CO;2.
6. L. P. Kopia, "Earth radiation budget experiment scanner instrument," *Rev. Geophys.* **24**(2), 400–406 (1986), http://dx.doi.org/10.1029/RG024i002p00400.
7. G. L. Smith et al., "Optical design of the CERES telescope," *Proc. SPIE* **4483**, 269–278 (2001), http://dx.doi.org/10.1117/12.453463.
8. F. O. Huck, N. Halyo, and S. K. Park, "Information efficiency of line scan imaging mechanisms," *Appl. Opt.* **20**(11), 1990–2007 (1981), http://dx.doi.org/10.1364/AO.20.001990.
9. F. O. Huck, N. Halyo, and S. K. Park, "Aliasing and blurring in 2-D sampled imagery," *Appl. Opt.* **19**(13), 2174–2181 (1980), http://dx.doi.org/10.1364/AO.19.002174.
10. S. J. Katzberg, F. O. Huck, and S. D. Wall, "Photosensor aperture shaping to reduce aliasing in optical-mechanical line-scan imaging systems," *Appl. Opt.* **12**(5), 1054–1060 (1973), http://dx.doi.org/10.1364/AO.12.001054.
11. N. D. Manalo and G. L. Smith, "Spatial sampling errors for a satellite-borne scanning radiometer," *Proc. SPIE* **1493**, 281–291 (1991), http://dx.doi.org/10.1117/12.46705.
12. N. D. Manalo, G. L. Smith, and B. R. Barkstrom, "Transfer function considerations for the CERES radiometer," *Proc. SPIE* **1521**, 106–116 (1991), http://dx.doi.org/10.1117/12.46068.
13. G. L. Smith, "Effects of time response on point spread function of a scanning radiometer," *Appl. Opt.* **33**(30), 7031–7037 (1994), http://dx.doi.org/10.1364/AO.33.007031.
14. M. P. A. Haeffelin, J. R. Mahan, and K. J. Priestley, "Predicted dynamic elctrothermal perfomance of thermistor bolometer radiometers for Earth radiation budget applications," *Appl. Opt.* **36**(28), 7129–7142 (1997), http://dx.doi.org/10.1364/AO.36.007129.
15. R. B. Lee, III et al., "Prelaunch calibrations of the cloud and the Earth's radiant energy system (CERES) tropical rainfall measuring mission and Earth Observing System Morning (EOS-AM1) thermistor bolometer sensors," *IEEE Trans. Geosci. Remote Sens.* **36**(4), 1173–1185 (1998), http://dx.doi.org/10.1109/36.701024.
16. J. Paden et al., "Reality check: point response function comparison of theory to measurements for the clouds and Earth radiant energy system (CERES) tropical rainfall measurement mission (TRMM) instrument," *Proc. SPIE* **3074**, 109–117 (1997), http://dx.doi.org/10.1117/12.280612.
17. J. Paden et al., "Point response function comparisons of theory to measurements for the clouds and the Earth's radiant energy system (CERES) TRMM (PFM), and the EOS AM (FM-1 & FM-2) instruments," *Proc. SPIE* **3439**, 344–354 (1998), http://dx.doi.org/10.1117/12.325640.
18. J. Paden et al., "Point response characteristics for the CERES/EOS-PM FM3 & FM4 instruments," *Proc. SPIE* **3750**, 395–406 (1999), http://dx.doi.org/10.1117/12.363536.
19. J. L. Daniels et al., "The measured point response functions of the CERES Flight Model 5 instrument," *Proc. SPIE* **8153**, 81531T (2012), http://dx.doi.org/10.1117/12.893677.
20. G. L. Smith et al., "Determination and validation of slow-mode properties of the clouds and the Earth's radiant energy system (CERES) scanning thermistor bolometers," *Proc. SPIE* **4135**, 25–38 (2000), http://dx.doi.org/10.1117/12.494226.
21. G. L. Smith et al., "Numerical filtering of spurious transients in a scanning radiometer: application to CERES," *J. Atmos. Oceanic Technol.* **19**(2), 172–182 (2002), http://dx.doi.org/10.1175/1520-0426(2002)019<0172:NFOSTI>2.0.CO;2.
22. K. J. Priestley, S. Thomas, and G. L. Smith, "Validation of point spread functions of CERES radiometers by the use of lunar observations," *J. Atmos. Oceanic Technol.* **27**(6), 1005–1011 (2010), http://dx.doi.org/10.1175/2010JTECHA1322.1.
23. J. L. Daniels et al., "The point response functions of CERES instruments aboard the Terra and Aqua spacecraft over the mission to date," *Proc. SPIE* **8515**, 85150O (2012), http://dx.doi.org/10.1117/12.928499.

G. Louis Smith received his BS, MS, and PhD in aerospace engineering from Virginia Polytechnic Institute. He has worked at Langley Research Center since 1956. He has published numerous journal articles and many conference papers. He received Langley's H.J.E. Reid Award for outstanding technical paper published at LaRC, the NASA Medal for Exceptional Scientific Achievement, and a Group Achievement Award for study, which led to the Earth Radiation Budget Experiment project.

Janet L. Daniels received her BS degree in mathematics with departmental honors from Christopher Newport University in 1991. After graduating from college, she became a mission operations specialist at NASA-Langley with HALOE from 1991 until 2005. She has been with the CERES team since 2005, first as a mission operations specialist and now as senior science analyst. She has received many company awards for outstanding achievement and group achievement awards for HALOE and CERES.

Kory J. Priestley received his BS in mechanical engineering from California Polytechnic State University-San Luis Obispo in 1992, then his MS in mechanical engineering in 1993 and PhD in 1997 from Virginia Polytechnic Institute and State University. He has worked at Langley Research Center since 1995. He is the instrument scientist for CERES. He has published numerous journal articles and conference papers. He was awarded the NASA Medal for Exceptional Achievement.

Susan Thomas is a lead scientist in the CERES Instrument group at NASA Langley Research Center. She received her BS in physics from University of Kerala, India, her MS in physics from University of Cochin, India, and her MS in computer science from Old Dominion University. She is involved in the CERES instrument operations, calibration, conversion algorithms, and validation. She has published many papers and has received NASA Group Achievement awards for her work on CERES.